Title

Non-isothermal melting of ice in the gas-diffusion layer of a proton-exchange-membrane fuel cell

Authors

Dursch, TJ
Trigub, GJ
Liu, JF
et al.

Publication Date

2013-12-01

DOI

10.1016/j.ijheatmasstransfer.2013.08.067

Peer reviewed

International Journal of Heat and Mass Transfer 67 (2013) 896–901

Contents lists available at ScienceDirect

International Journal of Heat and Mass Transfer

journal homepage: www.elsevier.com/locate/ijhmt

Non-isothermal melting of ice in the gas-diffusion layer of a proton-exchange-membrane fuel cell

T.J. Dursch [a,b], G.J. Trigub [a], J.F. Liu [a], C.J. Radke [a,c,*], A.Z. Weber [b]

[a] Chemical and Biomolecular Engineering Department, University of California, Berkeley, CA 94720, United States
[b] Environmental Energy Technology Division, Lawrence Berkeley National Laboratory, Berkeley, CA 94720, United States
[c] Earth Sciences Division, Lawrence Berkeley National Laboratory, Berkeley, CA 94720, United States

ARTICLE INFO

Article history:
Received 31 May 2013
Received in revised form 21 August 2013
Accepted 22 August 2013
Available online 21 September 2013

Keywords:
Stefan
Melting
Fuel cell
Gas-diffusion layer
Differential scanning calorimetry
Ice

ABSTRACT

Non-isothermal ice melting in the fibrous gas-diffusion layer (GDL) of a proton-exchange-membrane fuel cell (PEMFC) is investigated using differential scanning calorimetry (DSC). Non-isothermal ice-melting rates and ice-melting times are obtained from heat-flow measurements in water-saturated Toray GDLs at heating rates of 1, 2.5, 5, 10, and 25 K/min. In all cases, ice-melting times decrease nonlinearly with increasing heating rate. Nevertheless, melting temperatures remain at 272.9 ± 0.5 and 272.7 ± 0.4 K for bulk ice and ice within the GDL, respectively, reiterating that melting is thermodynamic-based at a rate limited by heat transfer. The slight GDL ice melting-point depression is consistent with the Gibbs–Thomson equation for equilibrium melting using an average pore diameter of 30 μm. Ice-melting endotherms are predicted from overall DSC energy balances coupled with a moving-boundary Stefan problem, where an ice-melting front within a GDL propagates with volume-averaged properties through an effective medium. Agreement between DSC experiment and theory is excellent. The proposed model accurately predicts ice-melting endotherms for Toray GDLs with two ice saturations and for bulk ice. Further, a pseudo-steady-state analysis obtains an analytical expression for ice-melting time, which is controlled by the time for heat addition to the propagating solid/liquid interface. Significantly, the new expression elucidates parameters controlling ice melting and allows for better design of both GDL materials and heating strategies to enhance the success of PEMFC cold-start.

Published by Elsevier Ltd.

1. Introduction

Proton-exchange-membrane fuel cells (PEMFCs) show promise in automotive applications because of their high efficiency, high power density, and potentially low emissions. In successful automotive applications, PEMFCs permit rapid startup from sub-freezing temperatures, known as cold-start. In a PEMFC, reduction of oxygen to water occurs in the cathode catalyst layer (cCL). Under subfreezing conditions, water solidifies and hinders access of gaseous oxygen to the catalytic sites in the cCL, severely inhibiting cell performance [1,2]. During cold-start, the time for recovering cell performance strongly depends on the rate of melting residual ice by reactive heat generation [3]. Elucidation of the mechanism and rate of ice melting within PEMFC-porous media is, therefore, critical to rapid cell startup and high performance at low temperatures.

Because of cell failure under subfreezing conditions, much attention has been given to understanding cold-start fundamentals. To date, experimental studies of PEMFC cold-start primarily focus on characterizing overall low-temperature cell performance including: degradation after freeze-thaw cycles [1], effects of cell material properties [2,4–6], and *in situ* visualization of ice formation [7]. Numerous studies show that the cell electrical potential decays rapidly at low temperatures due to ice formation at the reactive area of the cathode [1–8]. Currently, no studies focus on understanding the mechanism and rate of ice melting within PEMFC-porous media. Recently, several PEMFC cold-start models have been developed [3,8–11]. These models, however, adopt empirical melting rate expressions from ice-saturated-soil literature [12,13], since at this time one does not exist for PEMFC-porous media.

In the past few decades, significant effort has been expended on understanding melting both experimentally and theoretically because of the enormous variety of applications, including thermal energy storage using phase-change materials [14–17], metal casting [18–20], and polymer processing and sintering [21–23]. Numerous studies focus on melting of bulk ice [24–26] and ice within porous media [27–29], especially soils, rocks, and clays,

* Corresponding author at: Chemical and Biomolecular Engineering Department, University of California, Berkeley, CA 94720, United States. Tel.: +1 510 642 5204; fax: +1 510 642 4778.
E-mail address: radke@berkeley.edu (C.J. Radke).

0017-9310/$ - see front matter Published by Elsevier Ltd.
http://dx.doi.org/10.1016/j.ijheatmasstransfer.2013.08.067

Nomenclature

A_p	pan area containing DSC platform (m^2)
$\widehat{C}_p$	specific heat capacity (J/kg/K)
$\Delta\widehat{H}_f$	heat of fusion per mass of solid (kJ/kg)
k	thermal conductivity (W/m/K)
L	sample thickness (m)
m	mass (kg)
$\dot{Q}$	heat-flow rate (mW)
S	saturation
Ste	Stefan number
T	temperature (K)
T_o	273.15 K
t	time (s)
U	overall heat transfer coefficient ($W/m^2/K$)

Greek letters

α	thermal diffusivity (m^2/s)
β	heating rate (K/min)
δ	time-dependent ice/water interface position (m)
ε_o	GDL porosity
η	coordinate-transformed position in Eqs. (A1) and (A2)
ρ	mass density (kg/m^3)

Subscripts

C	carbon fibers
eff	effective
F	furnace
G	gas
L	liquid
O	initial
I	ice
p	pan
R	reference
S	sample

due to potential mechanical damage from frost heave. In nearly all cases [14–26], melting is described by a moving-boundary heat-transfer (Stefan) analysis. However, because the properties of fuel-cell materials differ considerably from soil media in wettability, pore size, and microstructure, proposed melting rates and mechanisms are not necessarily applicable.

This work measures and predicts non-isothermal ice melting in the fibrous GDL of a PEMFC. Ice melting is studied within the GDL because this layer is significantly ice saturated during PEMFC cold-start [3,7,10,11]. We use differential scanning calorimetry (DSC) to obtain non-isothermal ice-melting rates and ice-melting times as functions of heating rate for a commercial Toray GDL with two ice saturations and for bulk ice. We predict ice-melting endotherms by solving overall DSC energy balances coupled with the moving-boundary Stefan problem, where an ice-melting front within a GDL propagates with volume-averaged properties through an effective medium. Additionally, we utilize a pseudo-steady-state analysis to obtain an analytical expression for the time for complete ice melting. Notably, this expression elucidates parameters controlling ice melting and allows for better design of both GDL materials and heating strategies to enhance success of PEMFC cold-start.

2. Materials and methods

2.1. Sample preparation

Water-wetting TGP-H-060 carbon-paper GDLs were provided by Toray (Toray Corp., Tokyo, Japan). GDL samples were bored into 3.25-mm diameter circular disks and saturated with Ultrapure Milli-Q® (Millipore, Billerica, MA) distilled/deionized water in a home-built vacuum chamber for 1 h at 4.7 kPa. Following evacuation, excess surface water was removed by lightly blotting with Fisherbrand® weighing paper (Fisher Scientific, Pittsburgh, PA). GDL liquid-water saturations were controlled using a relative-humidity chamber [30]. Water content was determined gravimetrically; measured values were consistent with integrated peak areas generated from DSC. GDLs at two liquid-water saturations were studied: 20% and 85% [31]. Water loss by evaporation during DSC experiments was negligible. Additionally, capillary-pressure-saturation measurements showed that water does not drain from the GDLs under atmospheric pressure [32].

2.2. Differential scanning calorimetry

A PerkinElmer 6000 DSC (PerkinElmer Inc., Waltham, MA) with a liquid-nitrogen chiller measured sample heat-flow rate over time. The DSC was calibrated as described previously [31]. Nitrogen served as the purge gas at a flow rate of 20 mL/min. Water-saturated GDL samples, weighing between 1.4 and 2.2 mg, were placed into 20-μL PerkinElmer hermetically-sealed aluminum pans. For bulk-ice melting experiments, 8 or 19 μL of Ultrapure Milli-Q® distilled/deionized water was pipetted directly into 20-μL DSC pans. In all experiments, DSC pans were encircled by a 1-mm thick insulating polydimethylsiloxane (PDMS) ring to minimize radial heat loss. Non-isothermal melting was carried out over the temperature range of 273–300 K. Samples were placed into the DSC at 300 K, cooled to 235 K at 105 K/min, and held isothermally for 5 min. Following complete ice crystallization, samples were heated from 235 to 300 K at constant heating rates, β, of 1, 2.5, 5, 10, and 25 K/min. In all cases, $t = 0$ corresponds to the sample temperature, T_S, of 272 K.

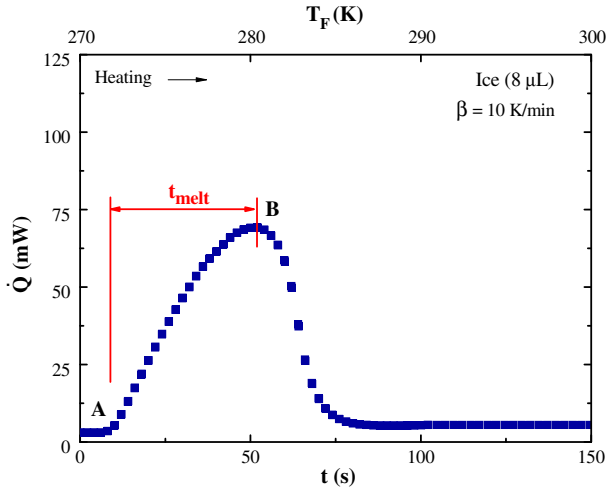

Fig. 1. Typical non-isothermal melting endotherm of heat-flow rate, $\dot{Q}$, vs. time, t, for bulk ice (8 μL) at a heating rate, β, of 10 K/min. A and B label the onset and completion of ice melting, respectively. The symbol t_{melt} defines the melting time. Furnace temperature, T_F, is shown in the upper abscissa.

3. Experimental results

Fig. 1 displays a typical melting endotherm of heat-flow rate, $\dot{Q}$ (mW), vs. time, t, for bulk ice (8 μL) at a heating rate, β, of 10 K/min. For reference, furnace temperature, T_F, is plotted on the superior abscissa. The sample was heated at 10 K/min from 235 to 300 K. For clarity, heat-flow rate is only shown from 272 to 300 K. Melting commenced at 10 s (point A in Fig. 1) corresponding to furnace and sample temperatures of 273.6 and 273.1 K, respectively. From point A, heat flow due to absorption of the enthalpy of melting is evident until complete melting is observed at point B, after which declining heat flow reflects the sensible heat necessary to raise the liquid-saturated sample temperature to the furnace temperature. Melting time, t_{melt}, is taken as that from melting onset to maximum heat-flow rate (point A–B), approximately 55 s in Fig. 1.

Fig. 2 shows measured melting endotherms of heat-flow rate vs. time for bulk ice (8 μL) at heating rates, β, of 1 (inverted triangles), 2.5 (circles), 5 (triangles), 10 (squares), and 25 K/min (diamonds). Lines in Fig. 2 are drawn according to theory discussed below. As β increases from 1 to 25 K/min, melting endotherms both narrow and reach greater peak heat-flow rates, consonant with identical water mass in each sample. Concurrently, the melting time, t_{melt}, decreases from 150 to 35 s. For all heating rates, however, the melting temperature is 272.9 ± 0.5 K corresponding to the melting point of bulk ice. This result suggests that melting is thermodynamic with a rate limited by heat transfer, in accordance with previous findings [14–29].

Similar measurements for two GDLs with varying ice saturation and a larger bulk ice volume (19 μL) were performed to quantify further the effect of β on the non-isothermal melting time, t_{melt}. Fig. 3 plots non-isothermal melting time, t_{melt}, as a function of heating rate, β, for a Toray GDL with ice saturations of 80% (open diamonds) and 19% (open squares), and 8 μL (filled triangles) and 19 μL (filled circles) of bulk ice. Solid and dashed lines correspond to theory, as described below. In all cases, t_{melt} decreases monotonically with increasing β. At a given β, t_{melt} is longest for 19 μL of bulk ice and is shortest for the ice-saturated GDLs, corresponding to 1.2 and 0.3 μL of ice. For all β, the melting temperature of ice within the GDL is 272.7 ± 0.4 K (near bulk ice), consistent with a slight melting-point depression calculated from the Gibbs–Thomson relation with an average pore diameter of 30-μm [32]. This result indicates that the large pore diameters do not significantly alter the equilibrium melting temperature of ice within a GDL compared to that of bulk ice.

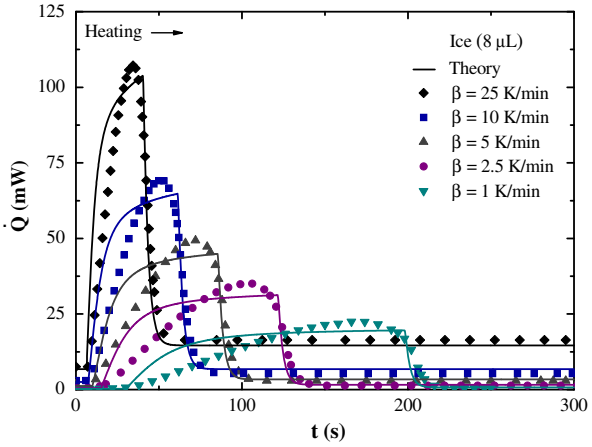

Fig. 2. Non-isothermal melting endotherms, $\dot{Q}$ vs. t, for bulk ice (8 μL) at heating rates, β, 1 (inverted triangles), 2.5 (circles), 5 (triangles), 10 (squares), and 25 K/min (diamonds). Lines are $\dot{Q}(t)$ predictions using Eqs. (1)–(4).

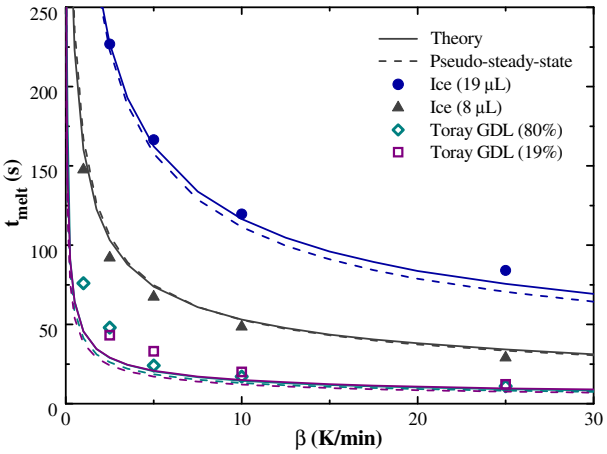

Fig. 3. Non-isothermal melting time, t_{melt}, as a function of heating rate, β, for a Toray GDL with two ice saturations 80% (open diamonds) and 19% (open squares), and 8 (filled triangles) and 19 μL (filled circles) of bulk ice. Solid lines are calculated using Eqs. (2)–(4), whereas dashed lines are calculated using Eq. (7).

4. Non-isothermal DSC theory

We desire quantitative prediction of DSC-measured ice-melting endotherms (i.e., heat-flow rate, $\dot{Q}$, vs. time, t). DSC heat-flow rate and sample temperature, $T_S(x,t)$, are determined by solving overall energy balances coupled with the moving-boundary Stefan problem [33].

Fig. 4 illustrates the simplified geometry for ice melting within an ice-saturated GDL of sample thickness L in a DSC pan insulated by a surrounding polydimethylsiloxane ring. At $x = 0$, heat supplied by the DSC furnace initiates ice melting at the equilibrium melting temperature, $T_S(\delta,t) = T_o$, where $\delta(t)$ denotes the time-dependent position of the advancing ice/water interface. For $x > \delta(t)$, sample temperature remains uniform at T_o during melting. For $x < \delta(t)$, however, $T_S(x,t)$ increases in time from heat supply by the DSC furnace. To establish the DSC-measured ice-melting endotherms, such as in Fig. 2 (i.e., $\dot{Q}(t)$), $T_S(x,t)$ and $\delta(t)$ must be specified.

Heat transfer within a DSC has been thoroughly investigated [34–37]. DSC sample and reference pans are encased in a temperature-controlled furnace. Upon heating, the furnace temperature, $T_F(t)$, is increased at a constant programmed rate, here linear, $T_F(t) = T_{Fo} + \beta t$, where T_{Fo} is initial furnace temperature and β is heating rate (K/min). Instrument-reported heat-flow rate is

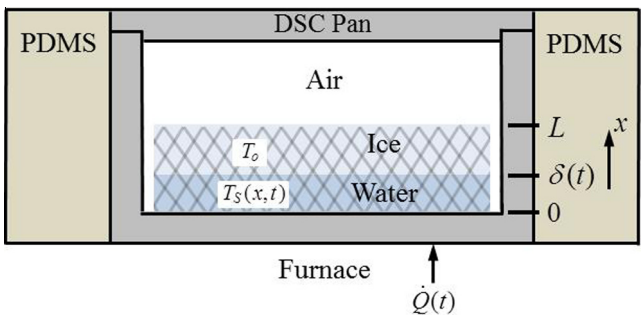

Fig. 4. Schematic for the 1-D DSC geometry. Cross-hatching indicates presence of a GDL. Symbols $\dot{Q}(t)$ and $\delta(t)$ label DSC heat-flow rate and time-dependent position of the ice/water interface, respectively. PDMS represents a 1-mm thick insulating polydimethylsiloxane ring. Drawing is not to scale.

proportional to the temperature difference between sample and reference pans [34]

$$\dot{Q}(t) = UA_p[T_R(t) - T_S(0,t)] \quad (1)$$

where U is the overall heat transfer coefficient, A_p is pan area in contact with the DSC platform, $T_R(t)$ is reference temperature, and $T_S(0,t)$ is sample temperature at the lower boundary of the sample pan in contact with the furnace.

As described previously [34], the product UA_p in Eq. (1) is obtained from DSC calibration using indium. Accordingly, $T_R(t)$ and $T_S(0,t)$ in Eq. (1) remain to be established. Following Eder [37], an overall energy balance describes the temperature of the reference pan

$$m_p \widehat{C}_{p,p} \frac{dT_R(t)}{dt} = UA_p[T_F(t) - T_R(t)] \quad (2)$$

where m_p and $\widehat{C}_{p,p}$ are pan mass and specific heat capacity, respectively.

To obtain $T_S(0,t)$, we adopt a 1-D moving-boundary Stefan problem [33], where a uniform liquid front propagates due to melting, at a rate limited by heat supply to the advancing solid/liquid interface. GDLs are highly porous carbon-fiber networks ($0.7 \leqslant \varepsilon_o$ (porosity) $\leqslant 0.9$ [31]) demanding that ice melts at a uniform equilibrium melting temperature, T_o. Accordingly, the progressing liquid front propagates with volume-averaged properties through an effective medium following a 1-D Stefan problem. $T_S(x,t)$ and $\delta(t)$ follow from liquid-phase and interfacial energy balances

$$\frac{\partial T_S(x,t)}{\partial t} = \alpha_{eff} \frac{\partial^2 T_S(x,t)}{\partial x^2} \quad 0 < x < \delta(t) \quad (3)$$

and

$$\rho_L \Delta \widehat{H}_f \varepsilon_o S_L \frac{d\delta(t)}{dt} = k_{eff} A_p \frac{\partial T_S(\delta,t)}{\partial x} \quad x = \delta(t) \quad (4)$$

where ρ_L is liquid mass density, $\Delta \widehat{H}_f$ is latent heat of fusion per unit mass of ice (taken as positive), ε_o is porosity (void volume per GDL volume), S_L is liquid-water saturation, and α_{eff} and k_{eff} are effective thermal diffusivity and conductivity, respectively. In Eqs. (3) and (4), we neglect natural convection in the melted region of the effective medium (i.e., a low Rayleigh number [38], radial conduction due to a GDL diameter-to-thickness ratio of over 20, and heat supply through the insulating air gap surrounding the GDL due to large thermal resistance. Effective properties in Eqs. (3) and (4) are calculated from liquid-phase, gas-phase, and carbon-fiber properties as $k_{eff} = S_L \varepsilon_o k_L + S_G \varepsilon_o k_G + (1 - \varepsilon_o) k_C$ and $\alpha_{eff} = k_{eff}/(\rho \widehat{C}_p)_{eff}$, where $(\rho \widehat{C}_p)_{eff} = S_L \varepsilon_o \rho_L \widehat{C}_{p,L} + S_G \varepsilon_o \rho_G \widehat{C}_{p,G} + (1 - \varepsilon_o) \rho_C \widehat{C}_{p,C}$, and subscripts L, G, and C denote liquid, gas, and carbon fiber, respectively. Accordingly, for ice melting in a DSC pan, $\varepsilon_o = 1$ and $S_L = 1$, giving $k_{eff} = k_L$.

Eq. (3) is solved numerically subject to the boundary

$$UA_p[T_F(t) - T_S(0,t)] = k_{eff} A_p \frac{\partial T_S(0,t)}{\partial x} \quad (5)$$

and

$$T_S(\delta,t) = T_o \quad (6)$$

Eq. (5) specifies continuity of heat flux at the GDL/furnace boundary while Eq. (6) sets the advancing ice/water interface temperature equal to the equilibrium melting temperature, T_o.

4.1. Numerical solution

To convert Eqs. (3) and (4) from a time-dependent to a time-independent domain, a Landau transformation is adopted [24], in which a new spatial variable is defined as $\eta(x,t) \equiv x/\delta(t)$. Eqs. (1) and (2), and coordinate-transformed forms of Eqs. (3) and (4) given in Appendix A are solved numerically in Matlab R2010a (The Math Works Inc., Natick, MA) using finite differencing and Newton iteration to resolve nonlinearities with a tolerance of 10^{-7}, a time step of 10^{-2} s, and 50 mesh elements. The inversion scheme BAND(j) solves resulting tridiagonal matrices [39]. In all cases, resulting $T_S(\eta,t)$ profiles are converted to the original coordinate systems $T_S(x,t)$ profiles based on calculated $\delta(t)$.

5. Discussion

5.1. Model comparison to experiment

Fig. 5 plots a representative sample-temperature profile, $T_S(x,t)$, calculated at times of 0, 40, 80, and 120 s for bulk ice (8 μL) heated at a rate of 2.5 K/min. From numerical solution of Eqs. (3)–(6), $T_S(x,t)$ increases in time due to continued heat supply from the DSC furnace and resulting conduction through the liquid-phase. Accordingly, $\delta(t)$ advances non-linearly in time as ice continues to melt, at a rate limited by heat addition to the ice/water interface. Since the time for heat addition to the propagating solid/liquid interface is limiting compared to the time for heat conduction through the effective medium, sample temperature is linear with position, as given by Eq. (B3) of Appendix B. In all cases, $T_S(0,t)$ is used to calculate $\dot{Q}(t)$ following Eq. (1).

Lines in Fig. 2 show predicted ice-melting endotherms of heat-flow rate, $\dot{Q}(t)$, vs. time for bulk ice (8 μL) at heating rates of β = 1, 2.5, 5, 10, and 25 K/min. All model parameters were independently evaluated and are listed in Table 1. Agreement is excellent between theory and experiment. With no adjustable parameters, the melting/heat transfer model quantitatively predicts $\dot{Q}(t)$ and t_{melt} for all β. Base-line heat-flow rate ($\dot{Q}(t)$, pre- and post-melting) increases linearly with β, as discussed elsewhere [34,35]. As expected, $\dot{Q}(t)$ during melting increases more rapidly with increasing β due to greater heat supply at the sample/furnace interface. Thus, as β increases from 1 to 25 K/min, predicted t_{melt} decreases monotonically.

The proposed melting/heat transfer model also accurately predicts $\dot{Q}(t)$ and t_{melt} for two GDLs with different ice saturations and for a larger bulk ice volume (19 μL). Solid lines in Fig. 3 are model predictions for t_{melt} (dashed lines are discussed below). For all β, melting kinetics of the ice-saturated GDLs are well-predicted using the 1-D Stefan problem with volume-averaged properties (i.e., an effective medium). Significantly, this result confirms that GDL ice melts at T_o in the highly-porous carbon-fiber

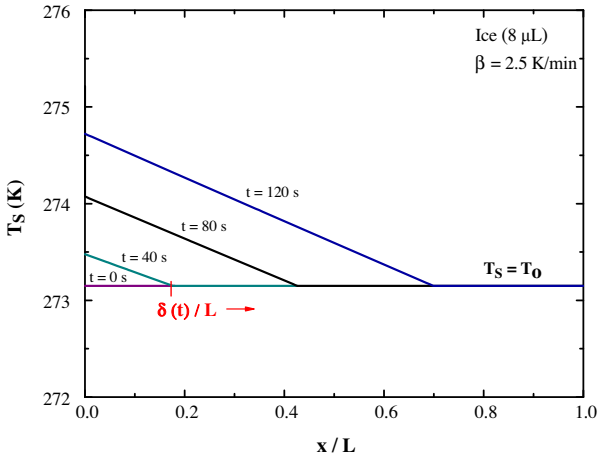

Fig. 5. Calculated sample-temperature profile, $T_S(x,t)$, at times of 0, 40, 80, and 120 s for bulk ice (8 μL) heated at a rate of 2.5 K/min. Symbols T_o and $\delta(t)$ label the equilibrium melting temperature and normalized time-dependent position of the ice/water interface, respectively.

Table 1
Model Parameters.

	Aluminum pan (p)	Water (L)	Carbon fibers (C)	Gas (G)
m (mg)	24.5	–	1.0	–
$\widehat{C}_p$ ($J\ kg^{-1}\ K^{-1}$)	910 [40]	4210 [40]	710 [11]	1000 [40]
k ($W\ m^{-1}\ K^{-1}$)	250 [40]	0.6 [40]	1.3 [41]	0.025 [40]
ρ ($kg\ m^{-3}$)	2700 [40]	990 [40]	490	1.2 [40]
L (μm)	–	–	190	–
UA_p ($W\ K^{-1}$)	0.035 [34]	–	–	–
A_p (mm^2)	9.6	–	–	–
$\Delta\widehat{H}_f$ ($kJ\ kg^{-1}$)	–	335.6 [40]	–	–
S_f	–	0.2, 0.85	–	0.8, 0.15
ε_o	–	–	0.8 [31]	–

matrix. Eqs. (3) and (4) constitute a new formalism to predict melting of ice within GDLs of varying ice-saturation during PEMFC cold-start (along with an appropriate heat transfer model).

5.2. Pseudo-steady-state ice melting

To elucidate parameters controlling t_{melt}, specifically β, we utilize a pseudo-steady-state analysis [24]. Eqs. (3) and (4) contain two time scales: the time for heat conduction through the effective medium and the time for heat addition to the propagating solid/liquid interface. When sensible heat is negligible compared to latent heat, i.e., low effective Stefan numbers ($Ste_{eff} = (\rho\widehat{C}_p)_{eff}(T_{Fo} - T_o)/\rho_L S_L \varepsilon_o \Delta\widehat{H}_f$), the time for movement of the advancing solid/liquid interface is rate limiting. Accordingly, the effective-medium temperature profile is pseudo-steady and linear as confirmed in Fig. 5; Eq. (3) simplifies considerably (see Appendix B). Under pseudo-steady-state conditions, pseudo-steady forms of Eq. (3) and Eqs. (4)–(6) are solved to obtain an explicit analytical expression for t_{melt}

$$t_{melt} = \left(\frac{\varepsilon_o \rho_L S_L \Delta\widehat{H}_f}{\beta}\right)^{1/2} \left(\frac{L^2}{k_{eff}} + \frac{2L}{U}\right)^{1/2} \tag{7}$$

where L denotes bulk-ice or GDL thickness. Fig. 3 compares effective medium (sold lines) and pseudo-steady (dashed lines) model-predicted t_{melt} vs. β for two GDLs with varying ice saturation (19% and 80%) and for two volumes of bulk ice (8 and 19 μL). As expected for bulk ice, t_{melt} decreases considerably with decreasing ice volume (V_I is related to sample thickness by $V_I = A_p L$). For the ice-saturated GDLs, however, t_{melt} is relatively insensitive to S_L, since effective thermal conductivity, k_{eff}, also decreases significantly with decreasing S_L. In all cases, excellent agreement indicates that Eq. (7) correctly scales with β, L, k_{eff}, S_L, and ε_o.

Eq. (7) permits design of both GDL materials and heating strategies to enhance the success of PEMFC cold-start. For example, from Eq. (7), t_{melt} is decreased using thinner, less porous, more-thermally conductive GDLs. However, Eq. (7) reveals two limiting t_{melt} contributions: conduction through (L^2/k_{eff}) and heat transfer to ($2L/U$) the GDL, elucidating that melting in even extremely thin, highly conductive GDLs is still limited by heat transfer to the GDL. Importantly, Eq. (7) allows optimization of t_{melt} through manipulation of material properties and heating strategies.

6. Conclusions

We determined ice-melting endotherms and ice-melting times as functions of heating rate in a fuel-cell gas-diffusion layer (GDL) using non-isothermal differential scanning calorimetry (DSC). Ice-melting rates were measured by DSC heat-flow dynamics for a commercial Toray GDL at two ice saturations and for bulk ice at heating rates of 1, 2.5, 5, 10, and 25 K/min. In all cases, ice-melting times decrease nonlinearly with increasing heating rate while melting temperatures remain 272.9 ± 0.5 and 272.7 ± 0.4 K for bulk ice and ice within the GDL, respectively. Accordingly, melting is thermodynamic-based with a rate limited by heat transfer. The slight GDL ice melting-point depression is consistent with the Gibbs–Thomson equation using an average pore diameter of 30 μm. Importantly, this result suggests that large pore diameters do not significantly alter the equilibrium melting temperature of ice within GDLs.

Ice-melting endotherms and ice-melting times are well-predicted from overall DSC energy balances coupled with a moving boundary. Since ice melts at the equilibrium melting temperature within the highly-porous GDL, we assume the ice-melting front propagates with volume-averaged properties through an effective medium following a 1-D Stefan problem. Agreement is excellent between theory and experiment. At all heating rates, the model accurately predicts ice-melting endotherms and ice-melting times for Toray GDLs with two ice saturations and bulk ice. To elucidate parameters controlling ice-melting times, we utilize a pseudo-steady-state analysis. For ice melting at low Stefan numbers, the time for heat addition to the propagating solid/liquid interface limits the process leading to an analytical expression for ice-melting time. Significantly, the proposed new expression allows for better design of both GDL materials and heating strategies to enhance the success of PEMFC cold-start.

Acknowledgements

This work was funded by the Assistant Secretary for Energy Efficiency and Renewable Energy, Fuel Cell Technologies Office, of the US Department of Energy under contract number DE-AC02-05CH11231.

Appendix A. Coordinate-transformed equations

To overcome the ice-melting moving boundary, we define the new dimensionless variable $\eta(x,t) \equiv x/\delta(t)$ [24]. Coordinate-transformed Eqs. (3) and (4) are

$$\delta^2(t)\frac{\partial T_S(\eta,t)}{\partial t} = \alpha_{eff}\frac{\partial^2 T_S(\eta,t)}{\partial \eta^2} + \delta(t)\eta\frac{\partial T_S(\eta,t)}{\partial \eta}\frac{d\delta(t)}{dt} \quad 0 < \eta < 1 \tag{A1}$$

and

$$\rho_L \Delta\widehat{H}_f \varepsilon_o S_L \delta(t)\frac{d\delta(t)}{dt} = k_{eff}\frac{\partial T_S(1,t)}{\partial \eta} \quad \eta = 1 \tag{A2}$$

Eq. (A1) is subject to the coordinate-transformed boundary conditions

$$UA_p\delta(t)[T_F(t) - T_S(0,t)] = k_{eff}A_p\frac{\partial T_S(0,t)}{\partial \eta} \tag{A3}$$

and

$$T_S(1,t) = T_o \tag{A4}$$

Appendix B. Pseudo-steady-state ice melting

To elucidate the limiting melting time scale, Eqs. (3) and (4) are non-dimensionalized to give

$$Ste_{eff}\frac{\partial T_S^*(x^*,t^*)}{\partial t^*} = \frac{\partial^2 T_S^*(x^*,t^*)}{\partial x^{*2}} \tag{B1}$$

and

$$-\frac{d\delta^*(t^*)}{dt^*} = \frac{\partial T_S^*(\delta^*,t^*)}{\partial x^*}, \tag{B2}$$

where $x^* = \frac{x}{L}$, $t^* = Ste_{eff}\frac{\alpha_{eff}t}{L^2}$, $T_S^* = \frac{T_S - T_o}{T_{Fo} - T_o}$, $\delta^* = \frac{\delta}{L}$, and $Ste_{eff} = \frac{(\widehat{\rho C_p})_{eff}(T_{Fo}-T_o)}{\rho_L S_L \varepsilon_o \widehat{\Delta H_f}}$ is the liquid-phase Stefan number within the effective medium, and T_{Fo} is furnace temperature at the melting onset. When sensible heat is negligible compared to latent heat, $Ste_{eff} \ll 1$. For ice melting within our fibrous GDL, Ste_{eff} is at most equal to 0.08 (for $T_{Fo} - T_o = 1$ K at $\beta = 25$ K/min). Thus, the left side of Eq. (B1) is neglected. Accordingly, Eq. (B1) solves analytically with boundary conditions $T_S^*(\delta^*,t^*) = 0$ and $Bi_{eff}\left[T_F^*(t^*) - T_S^*(0,t^*)\right] = \partial T_S^*(0,t^*)/\partial x^*$ to give

$$T_S^*(x^*,t^*) = \frac{Bi_{eff}T_F^*(t^*)}{1 + Bi_{eff}\delta^*}\left[\delta^* - x^*\right] \tag{B3}$$

where $Bi_{eff} = UL/k_{eff}$ is effective-medium Biot number and $T_F^*(t^*) = (T_F(t) - T_o)/(T_{Fo} - T_o)$. To solve for t_{melt}, Eq. (B2) is integrated from 0 to δ^*, with $T_F(t) = T_{Fo} + \beta t$ and $T_S^*(x,t)$ given by Eq. (B3), giving in dimensional form

$$k_{eff}\delta + \frac{U\delta^2}{2} = \frac{Ste_{eff}\alpha_{eff}U}{(T_{Fo} - T_o)}\left[(T_{Fo} - T_o)t + \frac{\beta}{2}t^2\right] \tag{B4}$$

Since $\beta t^2/2 \gg (T_{Fo} - T_o)t$ and $\delta(t_{melt}) = L$, Eq. (B4), after rearrangement, reduces to Eq. (7) of the text.

References

[1] C. Chacko, R. Ramasamy, S. Kim, M. Khandelwal, M. Mench, Characteristic behavior polymer electrolyte fuel cell resistance during cold start, J. Electrochem. Soc. 155 (2008) B1145–B1154.
[2] K. Tajiri, Y. Tabuchi, F. Kagami, S. Takahashi, K. Yoshizawa, C.Y. Wang, Effects of operating and design parameters on PEFC cold start, J. Power Sources 165 (2007) 279–286.
[3] R. Balliet, J. Newman, Cold start of a polymer-electrolyte fuel cell I. Development of a two-dimensional model, J. Electrochem. Soc. 158 (2011) B927–B938.
[4] M. Oszcipok, D. Riemann, U. Kronenwett, M. Kreideweis, M. Zedda, Statistic analysis of operational influences on the cold start behavior of PEM fuel cells, J. Power Sources 145 (2005) 407–415.
[5] S. Ge, C.Y. Wang, Characteristics of subzero startup and water/ice formation on the catalyst layer in a polymer electrolyte fuel cell, Electrochim. Acta 52 (2007) 4825–4835.
[6] X.G. Yang, Y. Tabuchi, F. Kagami, C.Y. Wang, Durability of membrane electrode assemblies under polymer electrolyte fuel cell cold-start cycling, J. Electrochem. Soc. 155 (2008) B752–B761.
[7] Y. Ishikawa, H. Hamada, M. Uehara, M. Shiozawa, Super-cooled water behavior inside polymer electrolyte fuel cell cross-section below freezing temperature, J. Power Sources 179 (2008) 547–552.
[8] L. Mao, C.Y. Wang, Y. Tabuchi, A multiphase model for cold start of polymer electrolyte fuel cells, J. Electrochem. Soc. 154 (2007) B341–B351.
[9] H. Meng, A PEM fuel cell model for cold-start simulations, J. Power Sources 178 (2008) 141–150.
[10] K. Jiao, X. Li, Three-dimensional multiphase modeling of cold start processes in polymer electrolyte membrane fuel cells, Electrochim. Acta 54 (2009) 6876–6891.
[11] R. Balliet, K.E. Thomas-Alyea, Water movement during freezing in a polymer-electrolyte-membrane fuel cell, J. Newman, ECS Trans. 16 (2008) 285–296.
[12] L. Bronfenbrener, E. Korin, Kinetic model for crystallization in porous media, Int. J. Heat Mass Transfer 40 (1997) 1053–1059.
[13] L. Bronfenbrener, E. Korin, Two-phase zone formation conditions under freezing of porous media, J. Cryst. Growth 198 (1999) 89–95.
[14] A. Sharma, V.V. Tyagi, C.R. Chen, D. Buddhi, Review on thermal energy storage with phase change materials and applications, Renew. Sustainable Energy Rev. 13 (2009) 318–345.
[15] B. Zalba, J. Marin, L.F. Cabeza, H. Mehling, Review on thermal energy storage with phase change: materials, heat transfer analysis, and applications, Appl. Therm. Eng. 23 (2003) 251–283.
[16] P. Lamberg, R. Lehtiniemi, A.-M. Henell, Numerical and experimental investigation of melting and freezing processes in phase change material storage, Int. J. Therm. Sci. 43 (2004) 277–287.
[17] F.L. Tan, S.F. Hosseinizadeh, J.M. Khodadadi, L. Fan, Experimental and computational study of constrained melting of phase change materials (PCM) inside a spherical capsule, Int. J. Heat Mass Transfer 52 (2009) 3464–3472.
[18] H. Hu, S.A. Argyropoulos, Mathematical modeling of solidification and melting: a review, Model. Simul. Mater. Sci. Eng. 4 (1996) 371–396.
[19] A.F. Albu, V.I. Zubov, Mathematical modeling and study of the process of solidification in metal casting, Comput. Math. Math. Phys. 47 (2007) 844–862.
[20] F. Stella, M. Giangi, Melting of a pure metal on a vertical wall: numerical simulation, Numer. Heat Transfer Part A 38 (2000) 193–208.
[21] J. Qu, G. Zeng, Y. Feng, G. Jin, H. He, X. Cao, Effect of screw axial vibration of polymer melting process in single-screw extruders, J. Appl. Polym. Sci. 27 (2006) 3860–3876.
[22] B. Crist, Small-angle X-ray scattering and polymer melting: a model study, J. Polym. Sci. Part B: Polym. Phys. 39 (2001) 2454–2460.
[23] A. Greco, A. Maffezzoli, Polymer melting and polymer powder sintering by thermal analysis, J. Therm. Anal. Calorim. 72 (2003) 1167–1174.
[24] V. Alexiades, A.D. Solomon, Mathematical Modeling of Melting and Freezing Processes, Hemisphere Publishing, Washington, D.C., 1993. pp. 155–160.
[25] T. Kousksou, A. Jamil, Y. Zeraouli, J.-P. Dumas, DSC study and computer modeling of the melting process in ice slurry, Thermochim. Acta 448 (2006) 123–129.
[26] T. Hirata, Y. Makino, Y. Kaneko, Analysis of close-contact melting of octadecane and ice inside isothermally heated horizontal rectangular capsule, Int. J. Heat Mass Transfer 34 (1991) 3097–3106.
[27] K. O'Neill, The physics of mathematical frost heat models: a review, Cold Regions Sci. Technol. 6 (1983) 275–291.
[28] X. Zhang, T.H. Nguyen, Melting of ice in a porous medium heated from below, Int. J. Heat Mass Transfer 34 (1991) 389–405.
[29] M. Kaviany, Principles of Heat Transfer in Porous Media, second ed., Springer-Verlag, New York, 1995. pp. 656–674.
[30] G.S. Hwang, A.Z. Weber, Effective-diffusivity measurement of partially-saturated fuel-cell gas-diffusion layers, J. Electrochem. Soc. 159 (2012) F683–F692.
[31] T.J. Dursch, M.A. Ciontea, C.J. Radke, A.Z. Weber, Isothermal ice crystallization kinetics in the gas-diffusion layer of a proton-exchange-membrane fuel cell, Langmuir 28 (2012) 1222–1234.
[32] J.T. Gostick, M.A. Ioannidis, M.W. Fowler, M.D. Pritzker, Wettability and capillary behavior of fibrous gas diffusion media for polymer electrolyte membrane fuel cells, J. Power Sources 194 (2009) 433–444.
[33] H.S. Carlsaw, J.C. Jaeger, Conduction of Heat in Solids, second ed., Oxford University Press, Oxford, 1959 (Chapter 11).
[34] T.J. Dursch, M.A. Ciontea, G.J. Trigub, C.J. Radke, A.Z. Weber, Pseudo-isothermal ice-crystallization kinetics in the gas-diffusion layer of a fuel cell from differential scanning calorimetry, Int. J. Heat Mass Transfer 60 (2013) 450–458.
[35] G.W.H. Hohne, W.F. Hemminger, H.J. Flammersheim, Differential Scanning Calorimetry, second ed., Springer, Heidelberg, 2003. pp. 31–63.
[36] G. Lamberti, Importance of heat transfer phenomena during DSC polymer solidification, Int. J. Heat Mass Transfer 41 (2004) 23–31.
[37] C.H. Wu, G. Eder, H. Janeschitz-Kriegl, Polymer crystallization dynamics, as reflected by differential scanning calorimetry. Part 2: Numerical simulations, Colloid Polym. Sci. 271 (1993) 1116–1128.
[38] W.M. Deen, Analysis of Transport Phenomena, first ed., Oxford University Press, 1998. pp. 488–493.
[39] J. Newman, K.E. Thomas-Alyea, Electrochemical Systems, third ed., John Wiley & Sons, 2004. pp. 614–619.
[40] F.P. Incropera, D.P. Dewitt, T.L. Bergman, A.S. Lavine, Fundamentals of Heat and Mass Transfer, sixth ed., John Wiley & Sons, 2007. pp. 928–951.
[41] E. Sadeghi, N. Djilali, M. Bahrami, Effective thermal conductivity and thermal contact resistance of gas diffusion layers in proton exchange membrane fuel cells. Part 1: Effect of compressive load, J. Power Sources 196 (2011) 246–254.